Journal of Rock Mechanics and Geotechnical Engineering xxx (xxxx) xxx

Contents lists available at ScienceDirect

Journal of Rock Mechanics and Geotechnical Engineering

journal homepage: www.jrmge.cn

Full Length Article

Deep learning-based temporal inference of hydraulic fracture length and branching using acoustic emission

Jian Liu [a], Omar AlDajani [b], Bing Qiuyi Li [c], Zili Li [a,b,*]

[a] Civil, Structural & Environmental Engineering, School of Engineering and Architecture, University College Cork, Cork, T12 K8AF, Ireland
[b] Department of Civil & Environmental Engineering, Massachusetts Institute of Technology, Cambridge, MA, 02139-4307, United States
[c] Department of Civil and Environmental Engineering, Western University, London, N6A 3K7, Canada

A R T I C L E I N F O

Article history:
Received 4 June 2025
Received in revised form
5 December 2025
Accepted 16 December 2025
Available online xxx

Keywords:
Hydraulic fracture
Acoustic emission
Fracture growth
Deep learning

A B S T R A C T

Acoustic emissions (AE) have been widely employed to infer fracture growth and cracking evolution in rocks and engineered structures. This study investigates the correlation between fracture growth – characterized by fracture length and the number of branches – and AE parameters, including counts, locations, and seismic moments, using deep learning (DL) approaches. A novel strategy is proposed that leverages spatiotemporal AE inputs from a historical period (L seconds) and a future timestep (Δt) to predict the incremental fracture length (IFL) and incremental number of fracture branches (INB) within each timestep. A customized DL model, termed AENet, is specifically designed to process the spatio-temporal AE inputs and predict IFL/INB, from which cumulative fracture growth metrics, including cumulative fracture length (CFL) and cumulative number of branches (CNB), are derived. Three hydraulic fracture experimental datasets from the MIT Rock Mechanics Laboratory are used to implement this DL-based correlation analysis. The results demonstrate that fracture growth exhibits a strong correlation with AE evolution, and the trained AENet model is capable of accurately predicting fracture growth from spatiotemporal AE data. Specifically, the AENet model (Δt = 1.0 s) achieves an average coefficient of determination (R^2) of 0.7512 and a mean relative error (MRE) of 0.3372 for CFL and CNB inference.

1. Introduction

Hydraulic fracturing is the most common engineering method for stimulating permeability in unconventional oil and gas reservoirs and in enhanced geothermal systems, where high-pressure fluid is injected into rock formations to generate high-permeability pathways (Economides and Nolte, 2000). It is well recognized that the density and complexity of the fracture network have a crucial influence on the production of oil or gas reservoirs (Li et al., 2022). Microseismic monitoring is widely used to map fracture growth and fracture complexity at field- and laboratory-scales (Maxwell et al., 2002). Microseismic events are also known as acoustic emissions (AE) at the laboratory-scale and are detected as transient elastic waves generated by the rapid release of strain energy within a material (Dresen et al., 2010). In the laboratory, AE parametric features were utilized to analyze failure behavior and to assess the cracking process and cracking level. AE parameters such as AE energy, counts, amplitude, rise time, average frequency, localization and duration were related to cracking process (Li et al., 2005; Moradian et al., 2010; Yang and Jing, 2011; Miao et al., 2018; Rodríguez and Celestino, 2019; Du et al., 2020; Cheng et al., 2023a,b; Qiao et al., 2024). AE counts and energy are straightforward to process and were initially analyzed to characterize the cracking process. Lockner (1993) reported the number of AE events was proportional to the number of growing cracks, and the energy of the AE signals was proportional to the magnitude of cracking event. They were also used to determine the cracking levels and different stages of rock damage evolution in uniaxial compression test. Li et al. (2005) investigated the cracking process of marble samples under uniaxial compression and found that the AE counts and cumulated AE counts reflect the initiation and propagation of cracks. Moradian et al. (2016) correlated AE hit rate and cumulative hits with the stress-strain

* Corresponding author. Civil, Structural & Environmental Engineering, School of Engineering and Architecture, University College Cork, Cork, T12 K8AF, Ireland.
E-mail address: zili.li@ucc.ie (Z. Li).
Peer review under responsibility of Institute of Rock and Soil Mechanics, Chinese Academy of Sciences.

https://doi.org/10.1016/j.jrmge.2025.12.046
1674-7755/

Please cite this article as: J. Liu, O. AlDajani, B.Q. Li *et al.*, Deep learning-based temporal inference of hydraulic fracture length and branching using acoustic emission, Journal of Rock Mechanics and Geotechnical Engineering, https://doi.org/10.1016/j.jrmge.2025.12.046

response of the specimens and then utilized it to determine the cracking levels in uniaxial compression experiments. Furthermore, moment tensor inversion (MTI) was adopted for AE source and focal mechanism analysis. AE localization is employed to assess fracture propagation, as AE events reflect the occurrence of microcracking, which typically develops within the process zone ahead of the crack tip. However, this remains challenging because AE events do not always fully correspond to the macroscale or visually observable fractures. Labuz et al. (2001) found that microcracks were not confined solely to the macroscopic failure planes, but also distributed outside the main fracture surfaces during fracture nucleation. Nevertheless, a strong correlation still exists between AE activity and observed fracture propagation. Multiple studies reported that fracture patterns corresponded with the AE locations when the confining pressure is high, and the stress level approaches residual stress after peak strength during uniaxial compressive tests (Labuz and Carvalho, 2000; Labuz et al., 2001; Chang and Lee, 2004). In hydraulic fracturing experiments, it is also observed that hypocenter locations of AE events correspond well with visually observed white patching (process zone) and crack patterns (Li et al., 2015, 2019). Li et al. (2019) summarized that the occurrence of many high-amplitude, dilative AE events over a short period of time indicates the coalescence of micro-cracks and the growth of macro-cracks. More recently, AlDajani (2022) quantified fracture length and branches of observed fracture networks in laboratory hydraulic fracturing experiments through real-time imaging monitoring, reporting a strong spatio-temporal correlation between AE parameters and fracture branching. In elastodynamic theory, AE waves are modeled as the response of a homogeneous medium generated by microcrack nucleation based on a dislocation model, where the crack volume is represented through the moment tensor (Ohtsu, 2022). Based on moment tensor analysis, relative crack volume can be obtained and used for analysis of damage evolution (Shigeishi and Ohtsu, 2001). Chang and Lee (2004) further suggested using AE sources associated with large relative crack volumes to accurately predict the major failure planes in rock. Numerical methods are also employed for modelling of seismicity and b-value analysis during cracking process (Zhao et al., 2014; Lei et al., 2021). However, the exact physical interpretation of simulated seismicity in coalescence of micro-cracks remains challenging. AE is numerically modeled as the failure of elements, where the seismic energy is estimated based on the released strain energy or the volume of the elements, from which the seismic moment of each event can be subsequently derived.

Developments in Deep Learning (DL) have helped geoscientists and geo-engineers reach a deeper understanding of coupled processes through data-driven discoveries and model-driven insights (Bergen et al., 2019). DL takes the form of building a model to recognize complex patterns and relationships between data and target variables. A built DL model f that represents a relationship between input x to a target y: $y = f(x)$, is optimized/trained using labeled training data (known data pairs including both the input x_i and corresponding label y_i). After that, a well-trained DL model can be used to predict targets from input x in unseen test data. Given that AE signals encompass complex time-frequency and positional information, DL offers significant advantages in analyzing such intricate data. DL has also shown considerable potential in many tasks based on analysis of AE signals, such as classification of loading scenario for rock fracture (Song et al., 2022), measurement of P wave arrival time and first-motion first motion polarity (Ross et al., 2018), estimation of the source focal mechanism (Kuang et al., 2021; Xie and Li, 2024) and identification of micro-seismic source event type (Dong et al., 2023). In addition to the direct use of AE waveforms, Sikdar et al. (2022) processed AE signals as time frequency scalogram data to classify and detect damage sources in a composite panel. Deep learning approaches facilitate the analysis of AE data (e.g., multidimensional matrices) in fracture mechanics as they are inherently well-suited for processing high-dimensional inputs.

In summary, the density and complexity of the fracture network have a crucial influence on the production of oil or gas reservoirs. Acoustic emissions (AE) are widely utilized for characterizing the cracking process and fracture propagation in materials and structures, and DL approaches show considerable potential for effectively processing AE data. To date, AE parameters are characterized and correlated with fracture geometry (Li et al., 2019), stress-strain behavior (Moradian et al. (2016)), and damage evolution (Shigeishi and Ohtsu, 2001) throughout the cracking process, thereby providing indications of fracture initiation, propagation, coalescence and the approximate direction of propagation. However, the precise relationship between the range of visible (macroscopic) fracture growth and AE characteristics remains unclear. There remains a limited investigation on quantitative relationship between AE and quantified fracture growth and complexity. This study applies a DL-based approach to investigate the relationship between hydraulic fracture growth, characterized by observed fracture length and branches, and spatiotemporal AE data. Based on the studies by Shigeishi and Ohtsu (2001) and Chang and Lee (2004), the time-series of AE event counts, source localization data, and seismic moments are selected as inputs. Section 2 introduces the hydraulic fracturing testing setup and data acquisition. Three hydraulic fracture experimental datasets are used in this study, including AE data and quantified fracture data from the Massachusetts Institute of Technology (MIT) rock mechanics laboratory. Section 3 presents data preparation and a novel inference strategy. The inference strategy is formulated using evenly sampled timesteps, in which the AE information from both a historical period (L seconds) and a short timestep (Δt) is utilized to predict the incremental fracture length (IFL) and the incremental number of fracture branches (INB) within that timestep. Additionally, a customized DL model, 'AENet', is developed to handle the spatiotemporal AE data and output IFL and INB. The AENet models were trained using two of the three datasets and test on the third. Finally, the test results of fracture growth and a parametric analysis on the inference method are demonstrated in Section 4.

2. Hydraulic fracturing experiments and data acquisition

2.1. Specimen preparation

The material used in the hydraulic fracturing tests is Opalinus shale. It is a clay-rich shale extracted from the Dogger Formation in the Jura Mountains, located in Northwest Switzerland, France, and Southern Germany. The Opalinus shale contains two distinct, alternating layers: a dark clay-rich material and a light quartz-carbonate mixed material. Detailed characterization of the specimens is discussed by AlDajani (2022). Three sets of hydraulic fracturing experiments were conducted on this shale at three distinct bedding plane orientations (30°, 45°, and 60° relative to the horizontally applied minimum principal stress). Fig. 1 shows different faces of an Opalinus shale specimen with a prefabricated central flaw (bedding orientation of 30°). The height, width, thickness, of the specimen were 100, 50, and 25 mm, respectively. A small thickness of the specimens is adopted for ensuring consistency of the specimen surface crack and internal damage (Miao et al., 2018). The length and width of the prefabricated central flaw were 10 mm and 2 mm, respectively.

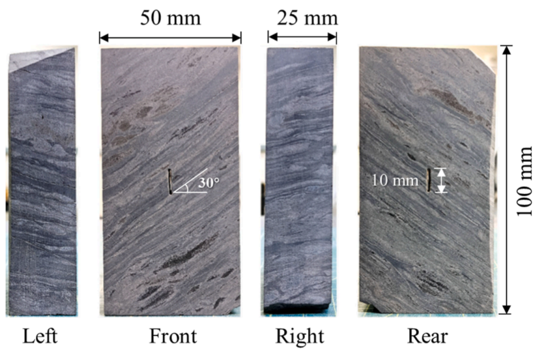

Fig. 1. Photographs of the 30° Opalinus shale specimen (AlDajani, 2022).

2.2. Test setup and procedures

AlDajani (2022) presents the hydraulic fracture testing apparatus at the MIT rock mechanics laboratory, as shown in Fig. 2. The testing setup and procedure is briefly described here. Especially, Fig. 3 shows the pressurization device. The main experimental steps are far-field loading, flaw saturation, and then pressurization:

(1) First, far-field biaxial loads are applied to a specimen containing a vertical pre-cut flaw and the clamping plate and acrylic housing apply a quasi-true triaxial stress state to the specimen. The specimen was seated by applying 0.3 MPa of axial and lateral load at 0.01 mm/s, and then loaded to 3 MPa and 1 MPa axially and laterally, respectively, at the same load rate of 0.05 MPa/s.
(2) Second, liquid is injected into the flaw until it is saturated. The liquid used is Mobil DTE-25, a hydraulic oil commonly used in pumps and other hydraulic systems using high pressure. At this stage, the injecting flow rates were around 5–15 μL/s, resulting in a flaw pressure spike of 0.5 MPa. The saturation stage resulted in a filled flaw without any flow through bedding.
(3) Finally, liquid is injected into the flaw at a constant flow rate (20 μL/s at the first pressurization stage then 105 μL/s at the second pressurization stage) to build up pressure and induce hydraulic fractures.

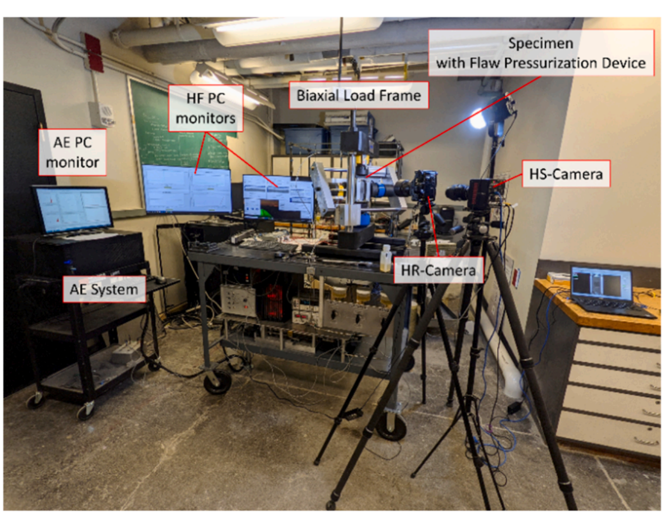

Fig. 2. Hydraulic fracture testing apparatus (AlDajani, 2022).

Tests end after the produced hydraulic fractures propagated to the edges of the specimen. For detailed experimental records, please see appendix B of AlDajani's thesis (2022).

2.3. Image and AE data acquisition

Real-time photographic monitoring and AE are widely used to investigate the cracking process (Li et al., 2005; Yang and Jing, 2011; Moradian et al., 2016; Miao et al., 2018; Du et al., 2020). It should be noted that both the visually observed fracture and AE results are interpreted under a two-dimensional (2D) assumption, wherein it is presumed that cracking and microcracking behavior is relatively uniform across the thickness of the rock specimen. This assumption is supported by previous studies (Miao et al., 2018; Li et al., 2019), which observed similar crack patterns on both the front and back surfaces, as well as in cross-sectional cuts of the specimens. This work utilizes data from the three sets of hydraulic fracture experiments, during which high-resolution images and AE data are simultaneously captured. The images of the cracking sequence were captured using a high-resolution Sony A7III camera and 90 mm macro lens recording at one frame per second. A total of 1049 high-resolution images from these experiments are used in this work. Also, continuous acoustic signals were monitored using eight PAC Micro30S sensors connected to a PCI-2 data acquisition system sampling at 5 MHz, as shown in Fig. 4. AE signals were detected using a sensor threshold of 35 dB by the eight P-wave acoustic sensors surrounding the rock, each recording the time of an event's occurrence and its amplitude. Subsequently, event locations and seismic moments were then inverted from these raw signal data according to the method of Li et al. (2019). Further details including analysis procedures, error analysis and processing program can be found in Section 6 of AlDajani's thesis (AlDajani, 2022).

2.4. Quantification of fracture growth

After the data collection, the growth of hydraulic fractures was quantitatively evaluated by the length and number of branches. As a descriptor of fracture growth, the cumulative fracture length (CFL) and cumulative number of fracture branches (CNB) are measured from fracture images (AlDajani, 2022). Fracture sketches are identified and extracted manually from raw fracture images using Photoshop. Subsequently, fracture sketches are skeletonized to measure the CFL and CNB to quantify the development of fracture growth (AlDajani, 2022). These quantities establish the ground truth of the spatiotemporal evolution of hydraulic fracture growth, which is observed indirectly as AE at the lab-scale. The development of fracture growth and distribution of AE events in three experiments are shown in Figs. 5–7. Figs. 5a, 6a and 7a show the images of final hydraulic fracture patterns from the three experiments. Figs. 5b, 6b and 7b show the manually extracted fracture sketches from the final fracture images. Figs. 5c, 6c and 7c show the localized AE event scatters, where the scatters are colored by time. It shows that the AE clusters distribute along the fracture branches. Additionally, a strong temporal relation between AE seismic moments (M_0) and the newly induced fracture length and branches can be observed in Figs. 5d, 6d and 7d. In the three experiments, AE frequently coincided with a significant increase in CFL and CNB. The 'fracturing peak' refers to the time period when observed fracture growth reaches peak (not the load peak in hydraulic fracturing test). It was observed that AE also occurred most frequently at fracturing peaks. Moreover, a steeper slope of the CFL or CNB curve corresponded to higher seismic moments. Dilative AE events with large seismic moments over a short period of time could indicate the growth of observed macro-

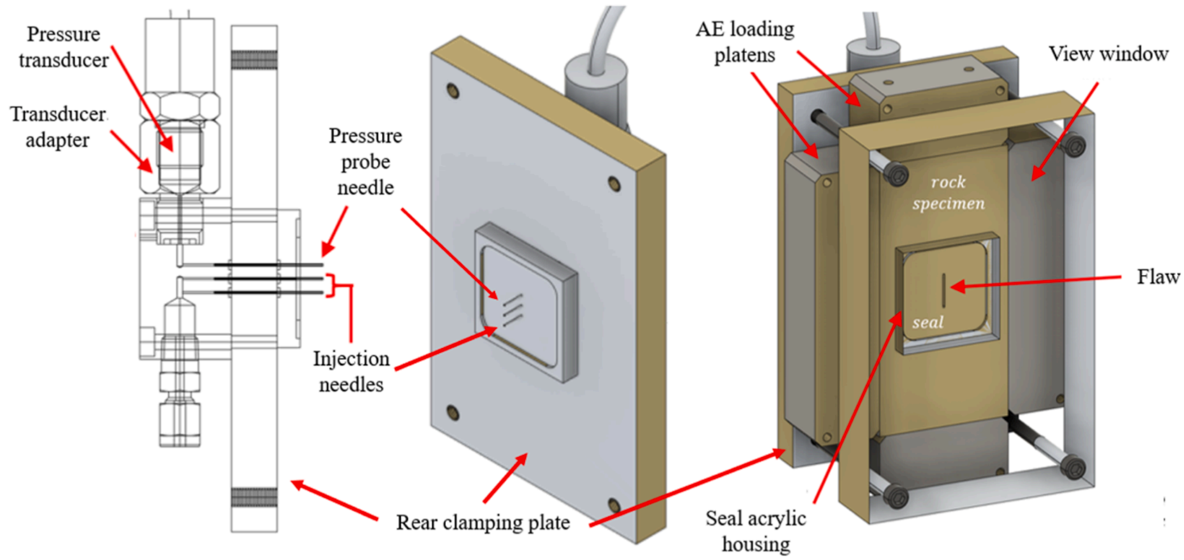

Fig. 3. Pressurization device (AlDajani, 2022).

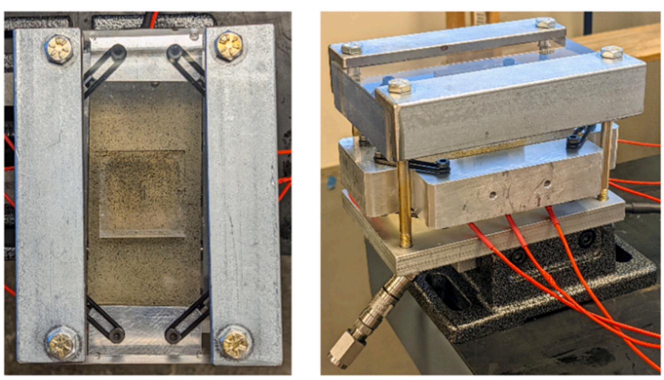

Fig. 4. AE sensors and AE platens installed onto the specimen (AlDajani, 2022).

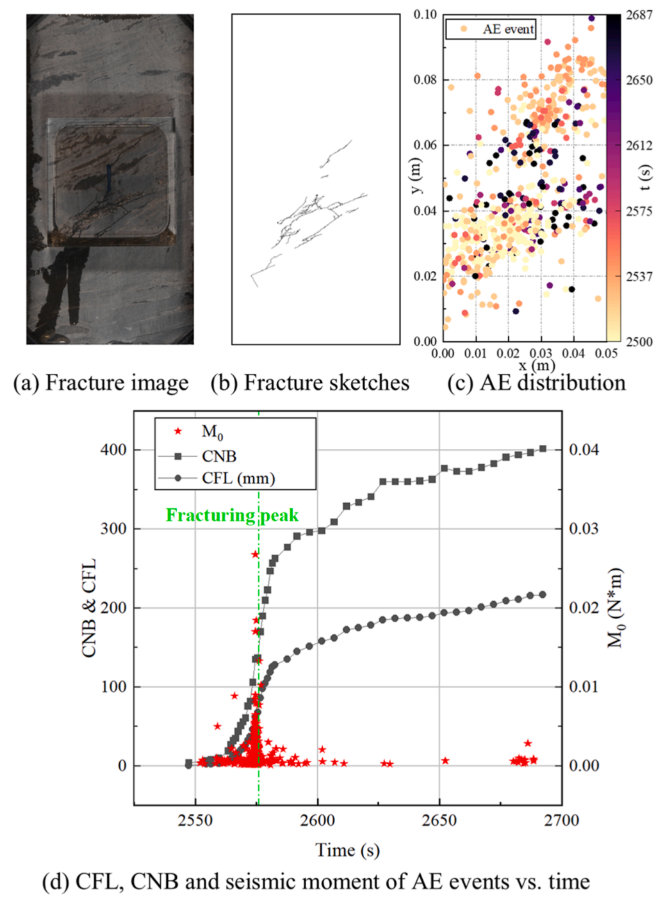

Fig. 5. Hydraulic fracture and AE events distribution (bedding orientation: 30°).

cracks. Inspired by this, the DL approaches were utilized to explore and model the hidden pattern between AE and fracture growth.

3. Data preparation and inference strategy

As mentioned in the introduction, a DL-method can model f that represents a relationship between input x to a target y: $y = f(x)$. In this study, a regression analysis is conducted between fracture growth (characterized by length and branches) and time-series AE parameters, including AE counts, event locations, and seismic moments. In this section, a dataset is prepared for DL model training consisting of n sample pairs (x_i, y_i) processed from AE data and structure fracture data. Firstly, AE data in a time period are processed as input x and the incremental fracture length (IFL) and incremental number of fracture branches (INB) within a time step as target y. Then, sample pairs are prepared according to an 'even timestep inference strategy'. In the proposed strategy, time series AE data in the historical time period is utilized to predict fracture evolution in a future timestep.

3.1. Fracture length and branch data

The IFL and INB targets within a timestep (Δt) are derived from CFL and CNB data. First, the CFL and CNB data shown in Figs. 5d, 6d and 7d are smoothed for denoising. The number of window points for smoothing is 5. Then, CFL and CNB curves are interpolated to obtain the IFL and INB in a short time step. Fig. 8 shows the processed IFL and INB data calculated over a 0.1 s timestep ($\Delta t = 0.1$s) and seismic moment (M_0) of individual AE events over the course of the three studied experiments. Note that longer timestep of 0.2 s

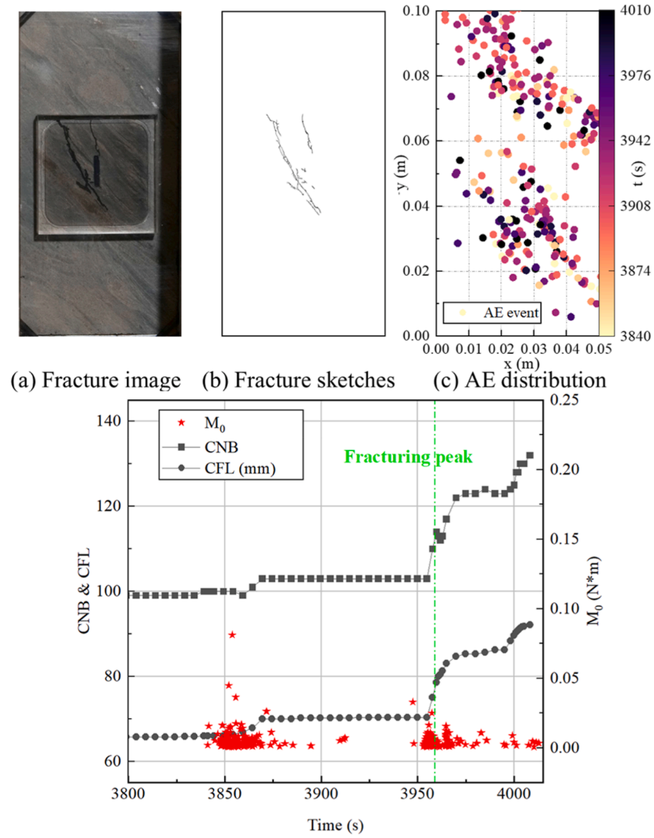

(a) Fracture image (b) Fracture sketches (c) AE distribution

(d) CFL, CNB and seismic moment of AE events vs. time

Fig. 6. Hydraulic fracture and AE events distribution (bedding orientation: 45°).

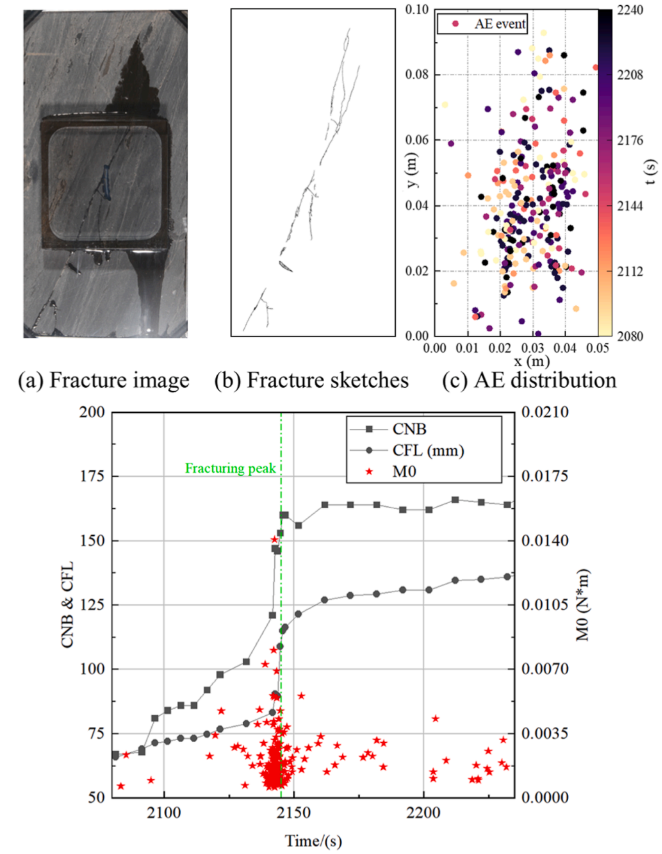

(a) Fracture image (b) Fracture sketches (c) AE distribution

(d) CFL, CNB and seismic moment of AE events vs. time

Fig. 7. Hydraulic fracture and AE events distribution (bedding orientation: 60°).

to 1 s are also explored in the results section. The value of IFL/INB at any given time T_n indicates the IFL or INB that occurred within the window T_n to $T_{n+1} = Tn + \Delta t$. Fig. 8 also shows all three experiments exhibit a strong correlation between the IFL/INB and the AE seismic moment, where IFL/INB and AE M_0 reach their peak values simultaneously during the fracturing peak. Moreover, greater IFL/INB increments correspond to AE event clusters with larger seismic moments.

3.2. Spatiotemporal AE data

Based on these observations and the study by Chang and Lee (2004), AE sources associated with large seismic moment may indicate the major failure planes in rock. The spatiotemporal characteristics of AE events –including event count, location, and seismic moment (M_0) – are related to IFL and INB, and can be utilized for their inference. Here, spatiotemporal AE data from the three laboratory experiments is characterized by 'AE maps' with time series. As shown in Fig. 9. The AE event locations are binned in space, and source times are binned in time to encode the spatiotemporal evolution of AE signals by using the AE map. The seismic moments of AE events are binned in 1 s windows and are mapped to 64*32-pixel grids, which is rescaled from the specimen size of 100 mm * 50 mm. The intensity of each grid cell in the AE map is calculated from the cumulative M_0 of AE events in that cell over a given 1 s window. This grid size is chosen given the relative sparsity of training data and to minimize the computational power required for training. In this case, the spatiotemporal evolution of AE including event seismic moment, location, source time, number of events are mapped/characterized by AE maps.

3.3. Inference strategy and dataset split

The preparation of input-target sample pairs is conducted based on an even timestep inference strategy. In this strategy, the IFL and INB in a fixed future timestep is predicted using an AE map sequence in a historical time. Fig. 10 illustrates the principle of the inference strategy, that the DL model predicts IFL/INB in the future timestep Δt at 'Tn' using spatiotemporal AE information in historical L seconds as well as a future timestep 'Δt'. As shown by the 'AE map sequence' in Fig. 10, the historical AE information is processed as a sequence of AE maps for DL model input, a 4D tensor with the size $(L+1) \times 1 \times 64 \times 32$ (sequence length × parameter numbers × height × width). The AE events within L s before Tn and those in the future Δt s are mapped using AE maps. For the historical AE events before Tn, AE events in a time window of L s are mapped every 1 s using L AE maps. While the last AE map involves the AE signals in the future Δt time period. In this case, the input 'Xn', the AE map sequence at the moment 'Tn' has L+1 AE maps (tensor sequence length: L+1), containing the AE temporal-spatial features in the historical L second and the future timestep Δt. Subsequently, it will be utilized to predict the targets 'Yn' (IFL/INB in Δt). As a result of data preparation, a sample pair including input 'Xn' and target 'Yn' is obtained. After data preparation based on the time series of the three experimental datasets, a total of 566 input–output sample pairs were obtained with a timestep (Δt) of 1 s. For the dataset prepared with a smaller timestep of 0.1 s, a total of 5660 input–output sample pairs were generated. The two datasets processed from experimental datasets (specimen with bedding orientations of 30° and 45°) ('30°' and '45°') were utilized

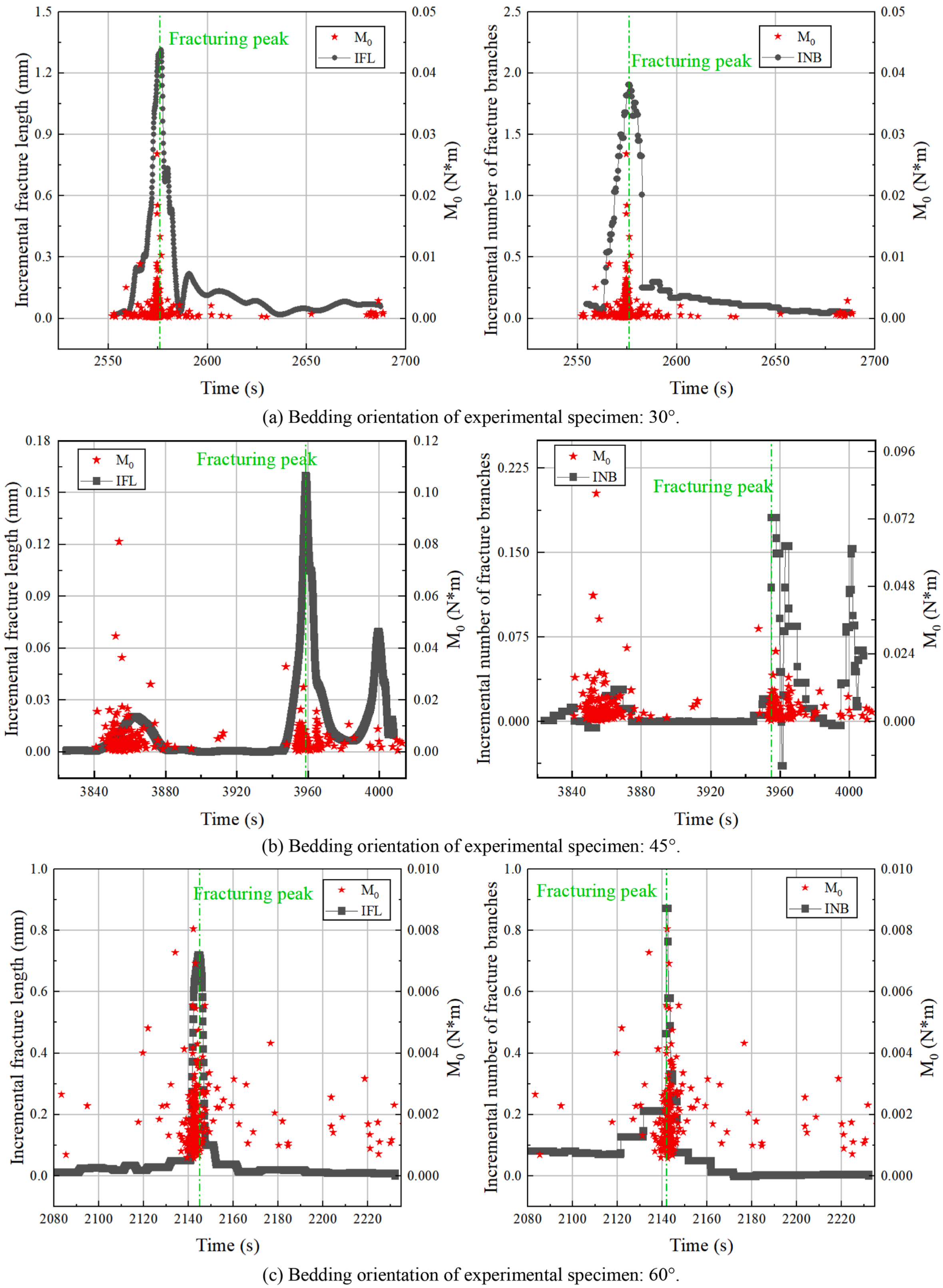

(a) Bedding orientation of experimental specimen: 30°.

(b) Bedding orientation of experimental specimen: 45°.

(c) Bedding orientation of experimental specimen: 60°.

Fig. 8. IFL and INB per 0.1 s and M_0 of AE events over time in three experiments.

as training data, while another dataset (bedding orientation: 60°) (‘60°’) as test data. Note that 20% of the experimental data from the ‘60°’ bedding angle experiment is utilized as validation data. From here, test data refer to dataset ‘60°’ that is not included in the training data sets.

A large dataset is typically required to robustly train DL models.

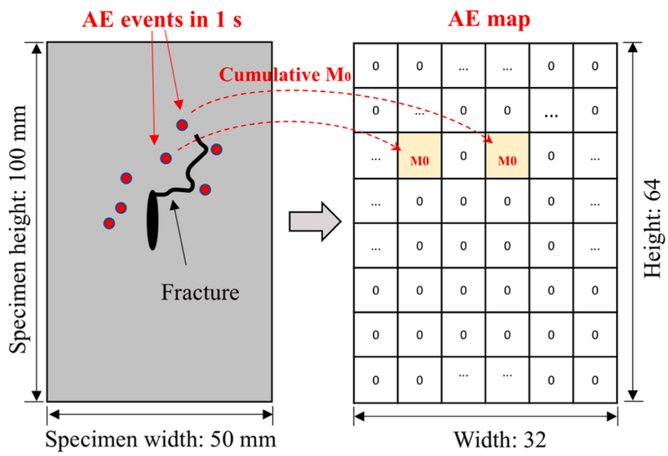

Fig. 9. Mapping of AE events using 'AE map' characterized by M_0.

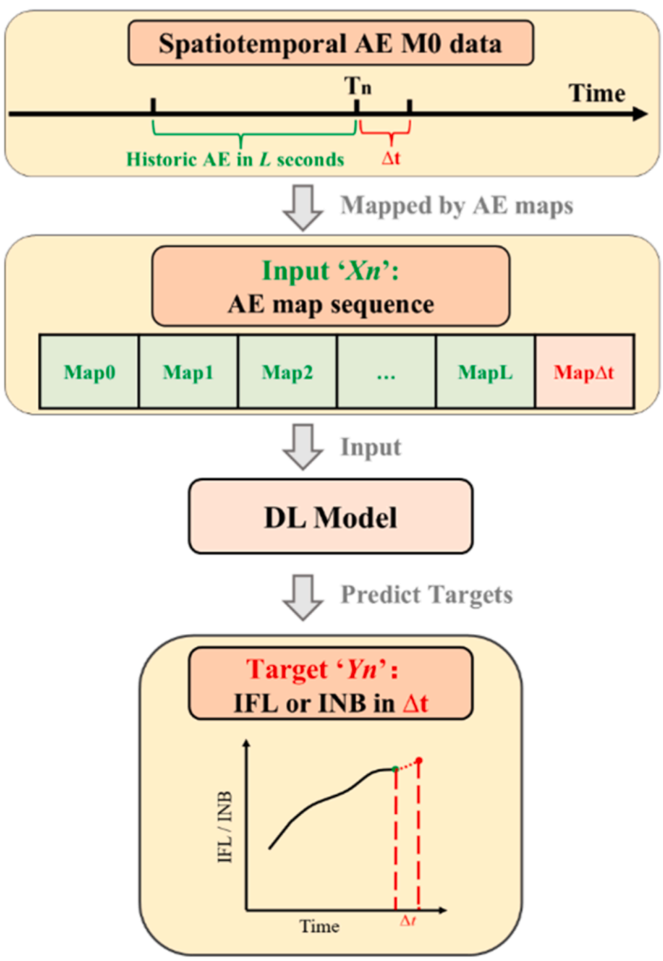

Fig. 10. Fracture growth inference strategy using AE information.

Therefore, the data are augmented by horizontally and vertically flipping the AE maps, given that the loading conditions are symmetric and thus fracture growth (fracture length and branches) does not depend on whether the specimen is flipped. This is illustrated in Fig. 11 and increases the size of the dataset fourfold, totaling 2264 samples (input-output pairs for timestep of 1 s) across the three experiments. When adopting 0.1 s timestep, the

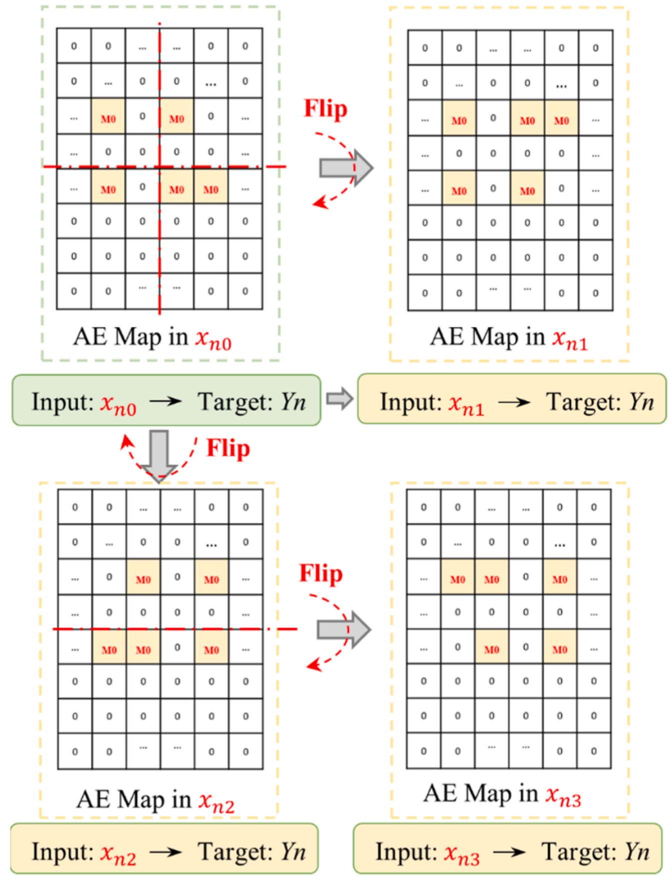

Fig. 11. Augmentation of input-target pairs by flipping AE maps vertically and horizontally.

dataset size is 22,640. These samples are normalized to a range of [0, 1] using minimum-maximum (Min-max) normalization before model training to ensure faster convergence and improve performance but not changing the final results. The normalization is expressed as:

$$x' = \frac{x - x_{\min}}{x_{\max} - x_{\min}} \tag{1}$$

where $x_{\max}$ is the maximum value in datasets, and $x_{\min}$ is the minimum value. x is the original value and x' is the normalized value.

4. Deep learning-based inference of fracture growth using AE

Deep Learning (DL) models represent the non-linear relationships and structures in datasets, specifically between data and target variables (Bergen et al., 2019). Inspired by this, the DL method is employed here to explore the quantitative relationship between:

(1) Produced fracture growth represented by fracture length and number of branches.
(2) Spatio-temporal evolution of AE represented by event source times, locations, numbers and seismic moment magnitude M_0.

This section presents a DL model to predict incremental fracture length (IFL) and incremental number of branches (INB) of hydraulic fractures using preprocessed AE maps. A DL model termed 'AENet' is designed and built to process temporal sequences of AE maps as input and predict IFL and INB. The overall DL-based inference workflow for IFL and INB inference is illustrated in Fig. 12. The major components of the workflow are:

(1) Data preparation: the IFL and INB over time are calculated from CFL/CNB data. These serve as the target of AENet. Meanwhile, the spatiotemporal evolution of AE is discretized using 'AE maps', where the AE event locations are binned and their source seismic moment M_0 is summed in each bin. The AE maps serve as the input data for the AENet and are binned in time similarly to the IFL and INB targets. Based on the inference strategy, input-target pairs are processed over a short timestep (Δt) at a given time *Tn*. As shown in Fig. 12, the AE information ($L+\Delta t$) over a historical time window L second and a timestep Δt are used as inputs to predict the IFL/INB in the current timestep. After data preparation, an input-target sample pair consists of the AE data over a time window of size $L+\Delta t$ and the target IFL/INB in the current timestep Δt. Three datasets are obtained after input-target pairs are processed from the three hydraulic fracturing experiments. Two of the experiments (Bedding orientation: 30° and 45°) are used as training data, and the third (Bedding orientation: 60°) for test data. Note that 20% of the experimental data from the '60' bedding angle experiment is utilized as validation data.
(2) DL model training: The DL model 'AENet' is trained and optimized on the training data. The architecture of AENet is described in Section 3.2.
(3) IFL and INB inference (model test): the trained AENet models are used to predict IFL/INB using the test data, and the predicted CFL and CNB over the course of the experiment can be calculated from the IFL/INB data. The performance can then be quantified between the inference and true CFL/CNB using measures such as mean absolute error (MAE) or the coefficient of determination (R^2).

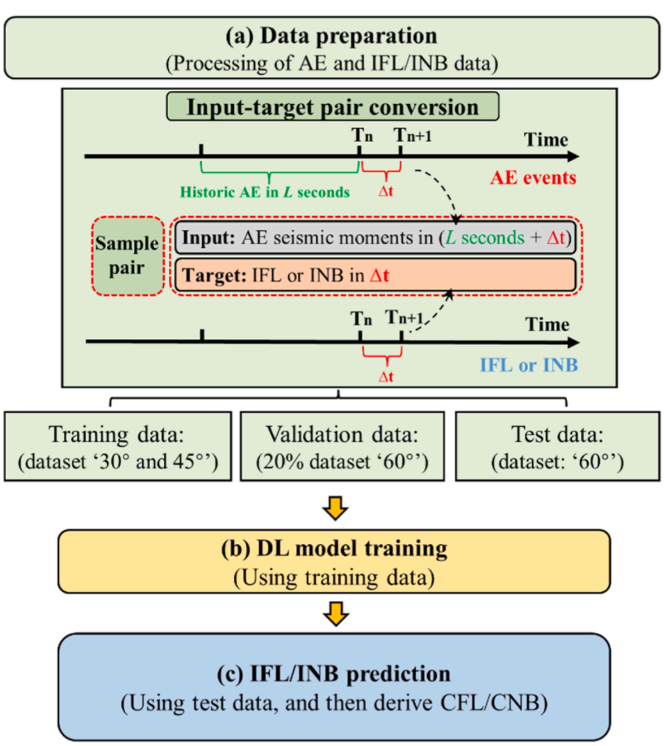

Fig. 12. DL method-based workflow of fracture growth inference using AE data.

4.1. 'AENet' architecture – from AE map to fracture growth

The choice of DL model architecture/structure is of great importance to explore the hidden pattern between AE and fracture data. In this study, a DL model named 'AENet' was developed and utilized to predict IFL/INB from AE data. This AENet consists of three main parts shown in Fig. 13. Firstly, convolutional layers are utilized for spatial feature extraction from AE maps. Convolutional neural network (CNN) is a class of artificial neural networks and is able to automatically and adaptively learn hierarchical spatial representations, from low-level to high-level patterns (Yamashita et al., 2018). Then, Long Short-Term Memory (LSTM) layers are employed to extract temporal features of the temporal AE map sequence (Yu et al., 2019). Finally, Fully Connected layers (FCs) are used to output the target. The full code implementing 'AENet' is available at: https://github.com/LJ-white/AENet-model.

In the first part of the AENet, CNN is employed to extract spatial features in the AE maps. A CNN unit consists of a convolutional layer and pooling layer (Yamashita et al., 2018). Average pooling gives emphasis on frequently occurring patches (AE events with similar seismic moments) in the input AE maps (Christlein et al., 2019). Since the AE events with large seismic moments may indicate major failure in rock (Chang and Lee, 2004), max pooling is employed for down sampling, aggregating AE features with larger intensity extracted from AE maps. An analysis of the impact of max pooling layers is provided in the Appendix. The commonly used residual connections are also included to expedite the training process (He et al., 2016). Residual connections are shown by the yellow dotted arrows in Fig. 14. For an input AE map sequence of size ((L+1) × 1 × 64 × 32) with a sequence length of 'L+1', each element (1 × 64 × 32) of the sequence is passed through a series of convolutional (residual) blocks and down sampled through the pooling layer. Fig. 14 illustrates the detailed structure of the CNNs, including 5 residual blocks. After the down-sampling operation, the dimensionality of an AE map (1 × 64 × 32) is reduced to a size of 32 × 8. The entire time sequence with the size of (L+1) × 32 × 8 is then passed to the LSTM.

In the second part, the LSTM block then processes the temporal evolution of the spatial AE features extracted from the convolutional layers (Yu et al., 2019). A LSTM layer is a recurrent unit, where recurrent cells update the current state based on past states and current input data. The sequence order of the AE map carries important temporal information of AE data. LSTM networks are well-suited for such data, as they maintain a memory of past inputs and are inherently sensitive to the temporal order of sequences. Thus, it can handle the time series features of historical AE information. An analysis of the impact of the LSTM layer is provided in the Appendix. LSTM can handle both long-term dependence problems and mitigates issues of vanishing

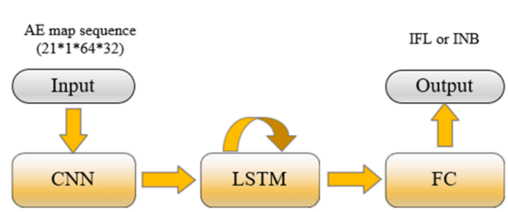

Fig. 13. Brief model architecture of AENet.

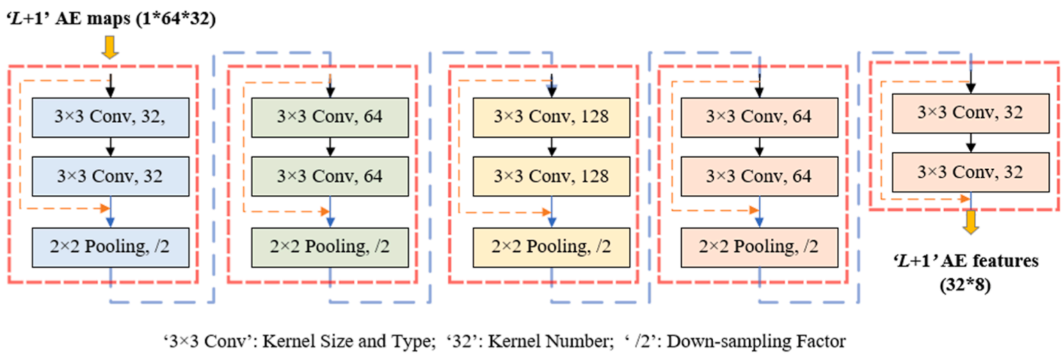

Fig. 14. Architecture of the CNN layers of AENet.

gradients (Zha et al., 2022). Fig. 15 shows the structure of the LSTM layers in AENet. The AE feature time sequence $(x_1, x_2, \ldots, x_{L+1})$ contains $L+1$ elements spaced over time and are fed into the LSTM block containing n layers. At each layer 'j', a LSTM cell h_i^j at state 'i' is updated based on the previous h_{i-1}^j after receiving input x_i.or h_i^{j-1}. In AENet, the LSTM block has a hidden size of $n = 128$ and just one layer. The LSTM module outputs the last state of the layer as a feature with dimension 1×128.

In the third part, Fully Connected (FC) layers are adopted to handle the entire spatio-temporal AE feature (tensor size: 1×128) from the LSTM layer to predict the target IFL/INB (Basha et al., 2020). FC layers connect every neuron in one layer to every neuron in the other layer. As shown in Fig. 16, the FC network consists of 5 layers, with 128, 64, 32, 16 and 1 nodes, respectively. Note that the IFL and INB are predicted from two different AENets with the same architecture after trained on train datasets, respectively.

4.2. Model training and optimization

Two AENet models ($L = 15$ s, $\Delta t = 1.0$ s), one for IFL inference and one for INB, are trained using the deep learning framework PyTorch using identical hyperparameters on a 'NVIDIA GeForce RTX 3050' GPU equipped with 8 GB of VRAM. The initial model

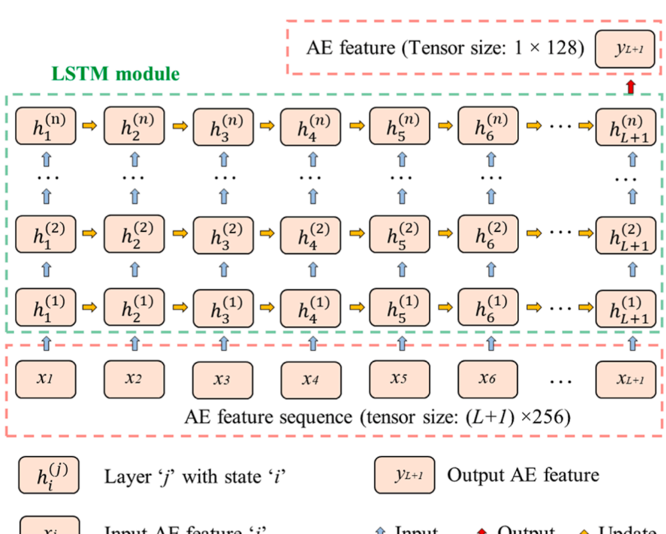

Fig. 15. Architecture of the LSTM layers in AENet.

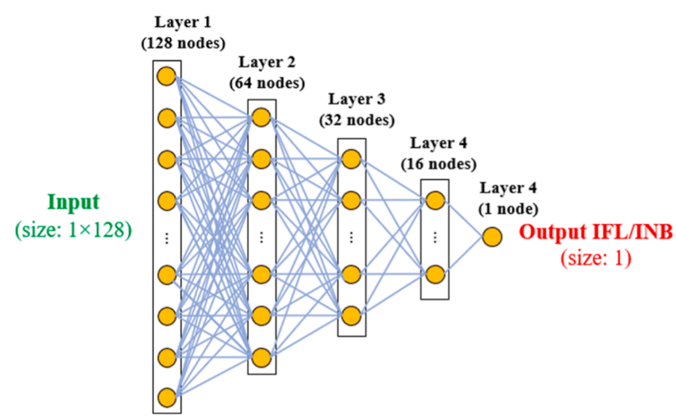

Fig. 16. Architecture of the FC layers in AENet.

hyper-parameters, including batch size, learning rate, weight initialization and number of training epoch are introduced in section 4.2. The batch size refers to the number of samples fed into the DL models in each epoch during training. The DL models are training over 20 epochs, with an initial learning rate of 0.0008 and a batch size of 32 selected through trial and error. The DL models are all trained to reach convergence after 20 epochs. The Adam optimizer (Kingma and Ba, 2014) is used to update the weights during model training. In addition, the overfitting can be solved by using 'L2' regularization and a discard rate of 0.0008 in the Adam optimizer. The Mean Squared Error (MSE) loss function is employed as the loss function (Yuan et al., 2021), defined as

$$MSE = \frac{1}{n}\sum_{1}^{n}(Y_i - \widehat{Y}_i)^2 \tag{2}$$

where n indicates the number of sample points; $\widehat{Y}_i$ is the predicted value and Y_i is the true value.

The two models for predicting IFL and INB were trained on their corresponding train data, during which training and validation errors were monitored. Fig. 17 illustrates the training and validation errors through 20 epochs. The AENet models exhibit convergence after 10 epochs. After 20 epochs, the training loss of the AENet model reaches 0.0002 when predicting IFL as the target, and the training loss reaches 0.0004 when predicting INB.

5. Results

This section presents the AENet inference results on the training and testing data using the proposed inference strategy, as

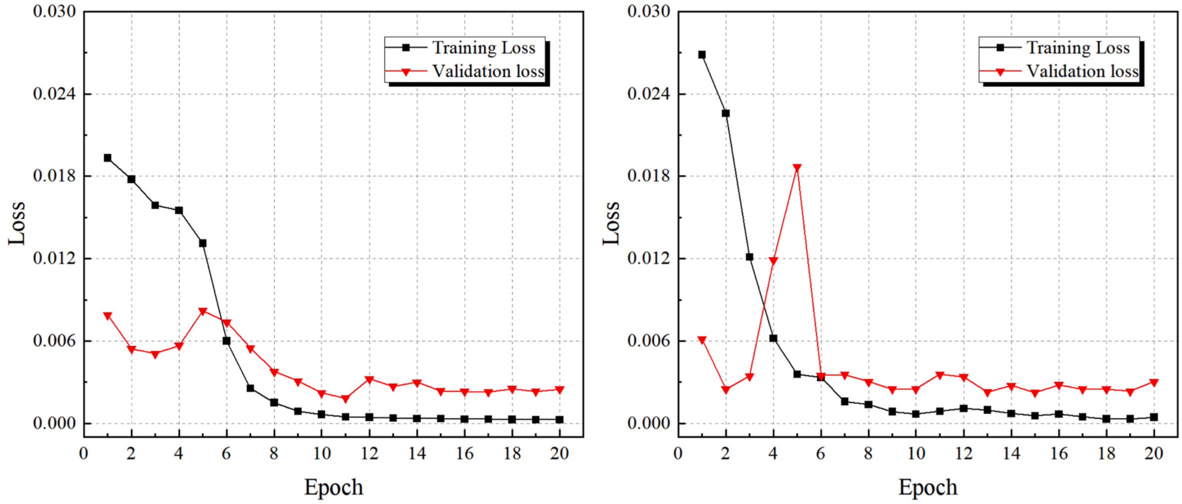

(a) IFL as target. (b) INB as target.

Fig. 17. Training loss and validation loss of AENet models.

well as a parametric analysis on lengths of the historical AE M_0 information and the inference timestep.

5.1. Evaluation on training data

The AENet model (L = 15 s, Δt = 1.0 s) learned the spatio-temporal relationship between fracture evolution represented by IFL/INB data and AE represented by time-series M_0 data. To evaluate the fitting performance of AENet on training datasets ('30°' and '45°'), the IFL/INB results over time obtained from AENet are evaluated based on experimental results, as well as the CFL/CNB results derived from IFL/INB results. Figs. 18 and 19 show the comparison between AENet inference of IFL/INB and corresponding ground truths on experiments with 30° and 45° bedding of specimens, respectively. Figs. 18a, c and 19a, c illustrate that the predicted IFL/INB over time exhibiting a consistency with ground truth on both datasets. The predicted IFL and INB can be integrated with respect to time and compared to corresponding CFL and CNB, as shown in Figs. 18b, d and 19b, d. The predicted CFL and CNB exhibit a consistent trend with the ground truth. This indicates the AENet models can capture the spatiotemporal relationship between AE M_0 and IFL/INB after learning on the training data.

5.2. Inference on test data

To evaluate the generalization ability of the trained AENet models, they are utilized to predict IFL/INB from AE data on the unseen test data. Fig. 20 compares the AENet inference to the ground-truth experimental results. Fig. 20a compares the IFL scatters over time, indicating the inferences from the AENet model are generally consistent with the true experimental results up to and including the fracturing peak point at 2145 s. The predicted results also reach the peak value of IFL at approximately the same time as the ground truth. The CFL/CNB overtime is derived from the IFL/INB. Consequently, the predicted and true CFL data are generally close before 2145 s of the experiment. Fig. 20b. Fig. 20c compares INB predicted by the AENet model to the true experimental results, again showing relatively good agreement with the true experimental result. The major misfits in the post-peak of CFL results as shown in Fig. 20b and d could be attributed to continued AE activity resulting from shear and tension along existing fractures rather than the initiation and propagation of more fractures as was observed experimentally (AlDajani, 2022).

The accuracy of the AENet inferences is also evaluated using Mean Relative Error (MRE) and coefficient of determination (R^2), which are commonly utilized for a robust measure of the inference results (Cameron and Windmeijer, 1997).

$$MRE = \frac{1}{n}\sum_{1}^{n}\left|\frac{Y_i - \widehat{Y}_i}{Y_i}\right| \quad (3)$$

where i indicates the number of sample points, $\widehat{Y}_i$ is the predicted value and Y_i is the real value.

$$R^2 = \frac{\sum_{1}^{n}|Y_i - \widehat{Y}_i|}{\sum_{1}^{n}|Y_i - \overline{Y}_i|} \quad (4)$$

where i indicates the number of sample points, $\widehat{Y}_i$ is the predicted value, Y_i is the real value and $\overline{Y}_i$ is the mean of the real data.

The evaluation of AENet inferences by MSE and R^2 is shown in Table 1, the AENet inference on test data (bedding orientation: 60°) achieved MSEs of 0.3157 mm^2, 1.0394 mm^2, 1.0394 and 303.1492 for IFL, CFL, INB and CNB. It also reaches a high a R^2 values of 0.8385 and for 0.6639 predicted CFL and CNB, exhibiting consistency with the ground truth shown in Fig. 20b and d. We see low MSEs on the training datasets, indicating good fitting performance of the model.

5.3. Parametric analysis

The DL algorithm captures and represents the pattern between input and target variables based on given training data. The selection of input and output variables significantly influences both the relationships modeled by the DL algorithm based on train data, and its inference performance on unseen test data. In the data preparation and inference strategy introduced in section 3.3, AE information (counts, location and seismic moment) from both a historical time window L and a future timestep Δt is used as input to predict fracture evolution (IFL and INB). To explore the robustness and scalability of the proposed DL inference strategy, this section presents a parametric analysis on the two parameters L

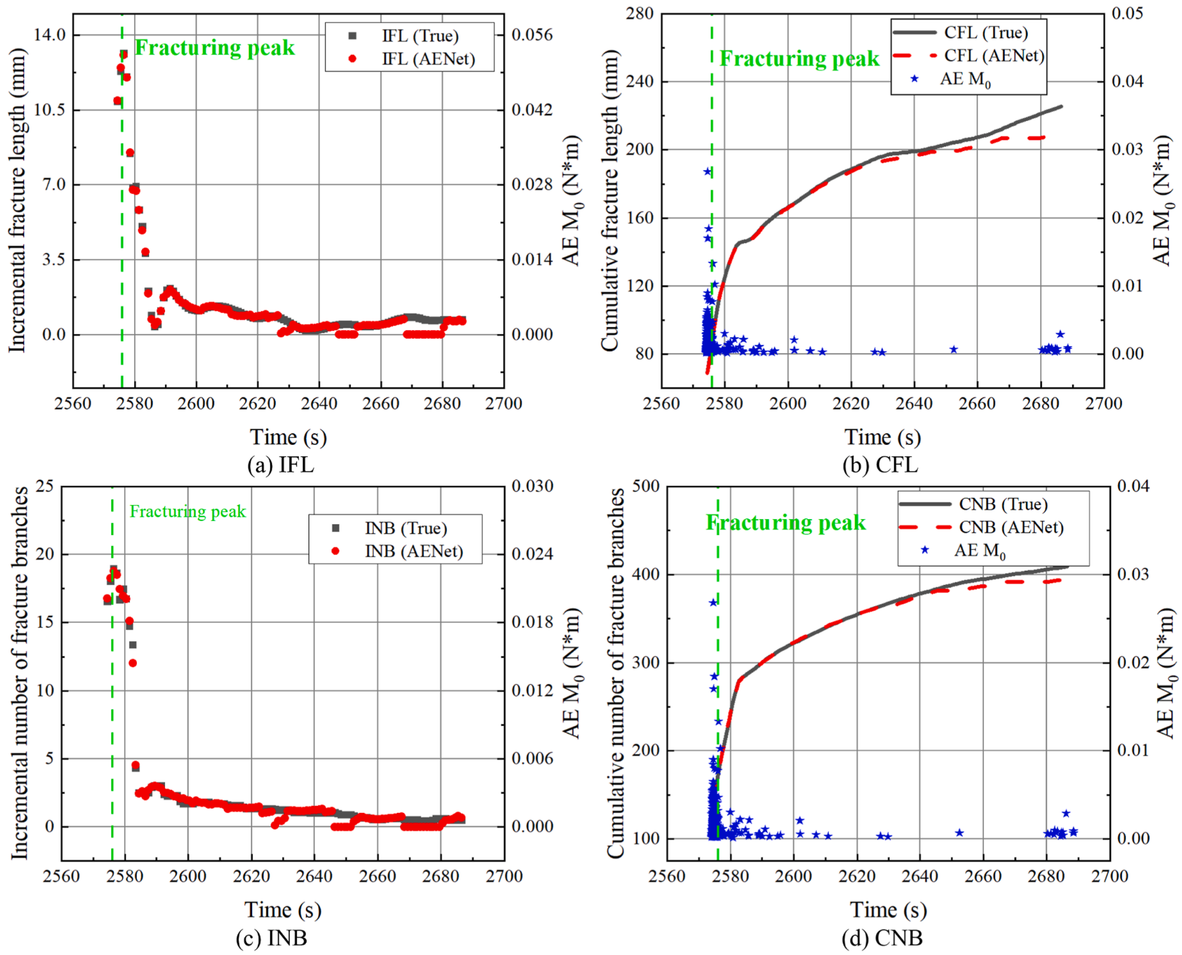

Fig. 18. Comparison of fracture length and branch development between AENet inferences and ground-truth experimental data (bedding orientation: 30°).

and Δt. Datasets with different L (0, 5, 10, 15, 20, 25 and 30 s) and Δt (0.2, 0.4, 0.6, 0.8 and 1.0 s) values are prepared and several AENet models are trained on these datasets following the procedures introduced as section 4.

5.3.1. *Length of historical time window (L)*

Datasets with L = 5, 10, 15, 20, 25 and 30 s are prepared to investigate the influence of the parameter L on predicting IFL/INB. The inference timestep is kept as 1 s (Δt = 1.0 s). Subsequently, these datasets are utilized to train AENet models and predict IFL and INB. The training of the models follows the same process introduced in Section 4.2, using the same hyperparameters. For predicting IFL/INB on each dataset (L = 5, 10, 15, 20, 25 or 30 s), the AENet model is trained on the training datasets ('30°' and '45°') and subsequently test on the test dataset ('60°'). The model training and testing process is repeated 10 times to obtain the average inference performance on each dataset (L = 5, 10, 15, 20, 25, or 30 s).

The MRE and R^2 are also used to evaluate the performances of AENet models on test data ('60°') with different values of L (5, 10, 15, 20, 25, or 30 s), as shown in Table 2. When adopting 15 s of L, the AENet model (Δt = 1 s, L = 15 s) achieves the best inference, reaching a highest average R^2 value of 0.7512 for predicting CNB and CFL. A high R^2 value indicates the model effectively captures most of the underlying patterns in the data and can make accurate inferences. It achieves MRE of 0.2853 on CFL inference and 0.3891 for predicting CNB. The results show that AENet model taking 15-s historical time window perform best. While longer or shorter L all reach low average R^2 value for CFL and CNB inferences.

Fig. 21 compares the predicted CFL and CNB over time (L = 5, 10, 15, 20, 25 and 30 s) with the real experimental results on test dataset (bedding orientation: 60°). As shown in Fig. 21a, the predicted CFL results show a significant consistency with the real experimental data up to and including the period of fracturing peak at 2145 s regardless of L. However, from 2140 to 2180 s, the CFL results with L values of 5, 10 and 30 s achieve higher inferences than the ground truth. After 2180 s, the CFL inference from models with L values of 20 and 25 s show an inconsistent increasing trend compared to the experimental results. Fig. 21b compares the predicted CNB results over time with the true experimental results. It shows a similar observation to the CFL results. The CNB predicted by models using L of 15 and 20 s are more consistent with the true data.

5.3.2. *Inference timestep (Δt)*

While L represents the historical time window, the inference timestep (Δt) represents the future time scale over which IFL/INB can be predicted using spatio-temporal evolution of AE signals. In this section, datasets with different inference timesteps (Δt = 0.2, 0.4, 0.6, 0.8 and 1.0 s) are prepared and utilized to train AENet models, respectively. The length of historical time window is set as 15 s (L = 15 s) based on the evaluation reported in Table 2. The AENet models are trained using the methodology described in Section 4.2.

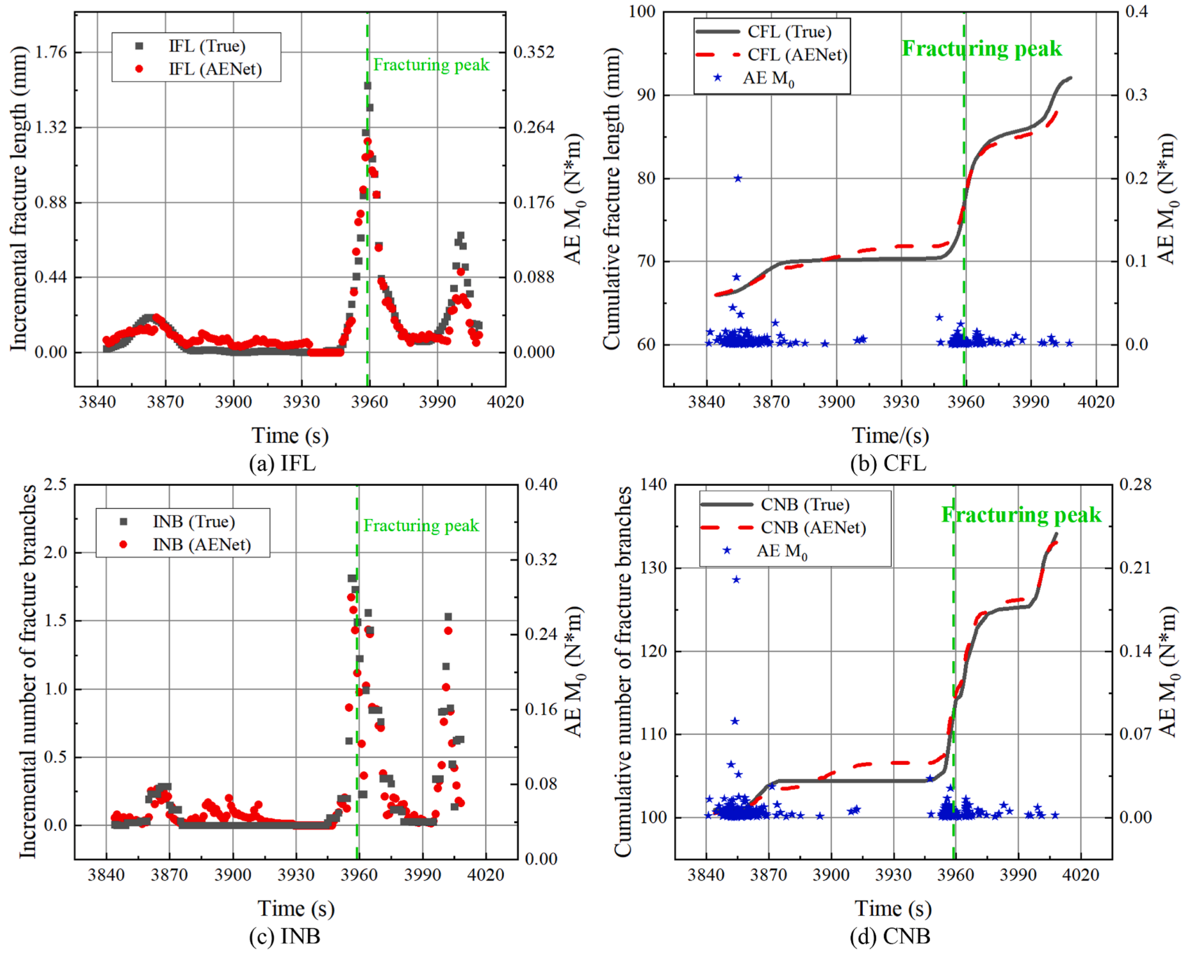

Fig. 19. Comparison of fracture length and branch development between AENet inferences and ground-truth experimental data (bedding orientation: 45°).

The MAE and R^2 evaluations of the AENet inferences on test data ('60°') adopting different Δt (0.2, 0.4, 0.6, 0.8 and 1.0 s) are shown in Table 3. The results indicate that AENet model achieves better inference performance when using a lager inference timestep. When using a 1.0-s inference timestep, AENet model (Δt = 1 s, L = 15 s) reaches the maximum average R^2 value of 0.7512 on CFL and CNB inference. When adopting a 0.2 s inference timestep, the AENet model (Δt = 0.2 s, L = 15 s) results a negative R^2 value. It indicates that the AENet model cannot reliably predict the IFL/INB on such a small timestep using AE data. When the inference timestep increasing from 0.2 s to 1.0 s, R^2 values of CFL and CNB increase, reaching 0.8385and 0.6639 respectively. Additionally, the MREs for CFL inference decrease as the inference timestep extends from 0.2 s to 1.0 s, dropping from 0.8578 to 0.2853. Also, MRE of CNB decreases from 0.7892 to 0.3891.

Fig. 22 compares the predicted CFL/CNB over time by AENet models with various inference timesteps (Δt = 0.2, 0.4, 0.6, 0.8 and 1.0 s) to the ground truth. As shown in Fig. 22a, after 2145 s of the experiment, as termed 'fracturing peak', the predicted CFL values are significantly higher than the true values. When inference timestep decreases from 1.0 s to 0.2 s, the deviations between AENet inference and the true experimental result become more significant. Fig. 22b compares the CNB inference results with the true experimental data. The results show a similar trend as the CFL results. The errors of predicted CNB curve by AENet increases as the inference timestep decrease from 1.0 s to 0.2 s.

6. Limitation and discussion

The micromechanics of AE associated with visible fracture initiation, propagation and coalescence in rocks is a highly complex topic. Observation of the cracking process with photography, together with AE monitoring, indicates that a relationship exists between these data streams. However, it is extremely difficult to decipher a clear pattern and establish a quantitative relationship. The primary objective of this work is to bridge the quantified fracture growth with the microcracks indicated by AE signals, and to identify key characterization factors through a DL-based analysis. It also provides a reference for the precise mapping of fracture complexity and branching in hydraulic fracturing in future studies. The visually observed fracture and AE results are interpreted under a 2D assumption, wherein it is presumed that cracking and microcracking behavior is relatively uniform across the thickness of the rock specimen. Though computed tomography (CT) scanning has the potential to achieve 3D characterization of crack inside the rock, it is limited to discrete specimens, whereas AE can be interpreted from fracture processes at any scale. The proposed AE map characterizes the spatiotemporal information of AE. The scaling ratio of the AE map can be set significantly large, which may help to mitigate the impact of localization inaccuracies caused by deficiencies in monitoring technology. Though the results indicate the DL has the potential to quantitatively model the relationship between fracture development and AE, some limitations remain:

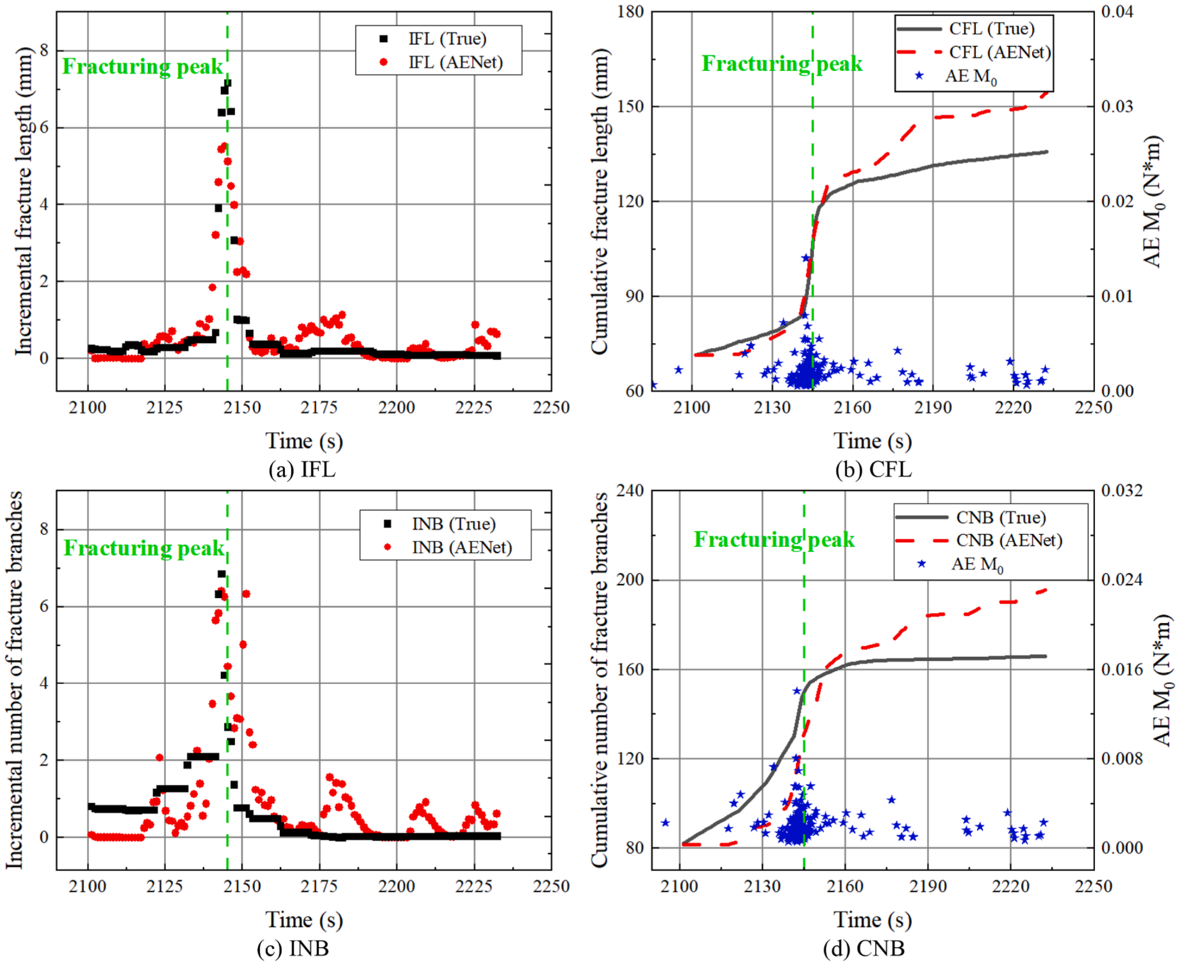

Fig. 20. Comparison of fracture length and branch development between AENet inferences and ground-truth experimental data (Test data with bedding orientation of 60°).

Table 1
MSE of inference results by AENet model (L = 15 s, Δt = 1.0 s).

Datasets	Mean squared error (MSE)				Coefficient of determination (R^2)	
	IFL (mm^2)	CFL (mm^2)	INB	CNB	CFL	CNB
Dataset '30°' (Train)	0.0865	31.3485	0.1399	37.4737	0.9681	0.9873
Dataset '45°' (Train)	0.006	1.1526	0.013	2.7845	0.9811	0.9715
Dataset '60°' (Test)	0.3157	100.5089	1.0394	303.1492	0.8385	0.6639

Table 2
MRE and R^2 of AENet inferences on test data adopting different L.

Length of historical AE M_0 information, L (s)	Mean relative error (MRE)			Coefficient of determination (R^2)		
	CFL	CNB	Average MRE value	CFL	CNB	Average R^2 value
5	0.4898	0.5842	0.537	0.5339	−1.0628	−0.2644
10	0.7433	1.0842	0.9138	−1.3252	−7.9552	−4.6402
15	0.2853	0.3891	0.3372	0.8385	0.6639	0.7512
20	0.2768	0.3325	0.3047	0.5735	0.7738	0.6736
25	0.5175	0.4129	0.4652	0.5501	−0.147	0.2016
30	0.6756	0.4121	0.5439	−0.1261	0.3963	0.1351

Note: Every MRE and R^2 is calculated from the average performance of 10 inference results. Each inference is made on the test data after an independent model training on the training data. The inference timestep (Δt) is 1 s.

(1) The proposed AENet demonstrates the potential to capture the spatiotemporal features of AE maps. While the appendix includes an analysis of the impact of LSTM and max pooling layers, a more comprehensive assessment of individual network components requires a larger and more diverse dataset.

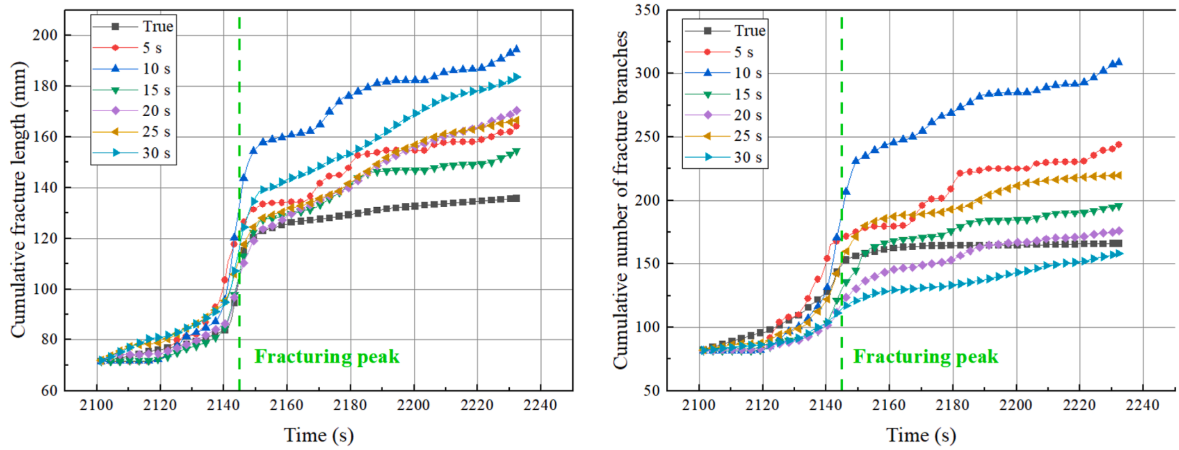

(a) CFL results (b) CNB results

Fig. 21. Comparison of true experimental results and AENet inference using different lengths of historical AE M_0 information (L = 5, 10, 15, 20, 25 and 30 s) (Test dataset: bedding orientation of 60°).

Table 3
MRE and R^2 of AENet inferences on the validation dataset adopting different timesteps Δt.

Inference timestep, Δt (s)	Mean relative error (MRE)			Coefficient of determination (R^2)		
	CFL	CNB	Average MRE value	CFL	CNB	Average R^2 value
0.2	0.8578	0.7892	0.8235	−2.4734	−2.8565	−2.665
0.4	0.8184	0.7049	0.76165	−2.9040	−1.8057	−2.3549
0.6	0.6406	0.4322	0.5364	−1.0615	0.4168	−0.3224
0.8	0.4819	0.5814	0.5317	0.2982	−0.7485	−0.2252
1.0	0.2853	0.3891	0.3372	0.8385	0.6639	0.7512

Note: MRE and R^2 are calculated from the average performance of 10 inference results. Each inference is made on the test data after an independent model training on the training data. L = 15 s in all cases.

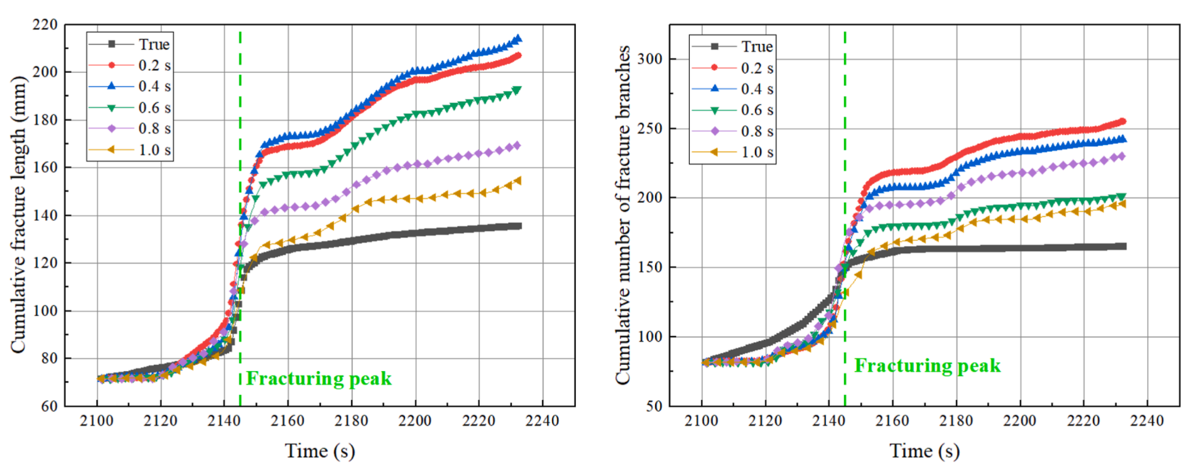

(a) CFL results (b) CNB results

Fig. 22. Comparison of ground-truth experimental results and AENet inference adopting different inference timesteps (Δt = 0.2, 0.4, 0.6, 0.8 and 1.0 s) (Test dataset: bedding orientation of 60°).

(2) The training and test datasets from the three experimental sets involve rock specimens (Opalinus shale) with the same geological origin, fabric, mechanical properties, pre-loading pressure, and pressurization procedure. These factors were not explicitly incorporated into the deep learning model or dataset, though it was observed the AE parameters are influenced by rock fabric and stress history (Carpinteri et al., 2013; Rodríguez and Celestino, 2019). We hope more researchers join in expanding the model validation and advancing related modeling approaches in the future.

(3) Moreover, many AE parameters are related to the cracking process in previous studies. In this study, the time-series of AE event counts, source location and seismic moments are selected as inputs based on the studies by Shigeishi and Ohtsu (2001) and Chang and Lee (2004). The other parameters could be investigated by characterizing their

spatiotemporal cumulative effects based on this model, such as role of the AE focal mechanism (shear vs tensile events) in predicted fracture growth.

7. Conclusions

This study investigates the relationship between the quantified growth of hydraulic fracture and spatio-temporal AE data using a Deep Learning approach. A inference strategy and a customized Deep Learning model, termed 'AENet' is developed to explore the pattern between AE parameters (counts, location and seismic moment) and fracture growth (length and branches). Specifically, the AE data are binned into a rolling window in time over a historical period (L seconds) and a future timestep (Δt) to predict the IFL and INB at that timestep. Three datasets containing both AE and quantified fracture data from three hydraulic fracturing experiments on Opalinus shale specimens, are used to develop and validate the proposed method. The two datasets from experiments on specimens served as training data, while another dataset is used for model testing. The main findings are summarized as follows:

(1) The DL model AENet quantitatively captures the spatio-temporal relationship between microseismic activity represented by AE counts, location and M_0 and quantified fracture growth represented by IFL and INB. After model training, the model can achieve consistent CFL and CNB inferences with ground-truth experimental datasets with specimen bedding orientations of 60° (test data). These inferences are valid up to and including the fracturing peak, after which the inference diverges from the ground truth, which may be attributed to continued shearing and opening along previously created fractures. Many of the AE produced during the '60°' experiment occurred on existing fractures resulting in the model overestimating fracture growth post peak fracturing (after 2160 s).

(2) The length of the time window containing historical AE M_0 data (L) and inference timestep (Δt) have a significant influence on the inference performance. The parametric analysis indicates that adopting L values within 15 s offers the best inference, reaching a R^2 of 0.7512. The AENet model ($L = 15$ s and $\Delta t = 1.0$ s) achieves an average MRE of 0.3372 for CFL and CNB inference. This may be attributed to the development of the process zone prior to the initiation of the fractures, which is reflected in the AE source locations and provides an area of reduced fracture resistance for the eventual fracture propagation. Additionally, the model inferences become increasingly less accurate when using shorter timesteps. As the inference timestep decreases from 1.0 s to 0.2 s, predicted CFL/CNB results are significantly overestimated compared to the ground-truth experimental result. This is consistent with the current understanding that the observed fracture is the result of the cumulative microcracks indicated by AE activity.

CRediT authorship contribution statement

Jian Liu: Writing – original draft, Software, Investigation, Formal analysis. **Omar AlDajani:** Writing – review & editing, Supervision, Formal analysis, Data curation. **Bing Qiuyi Li:** Writing – review & editing, Validation, Supervision, Investigation. **Zili Li:** Writing – review & editing, Supervision, Project administration, Investigation, Funding acquisition, Conceptualization.

Declaration of competing interest

The authors declare that they have no known competing financial interests or personal relationships that could have appeared to influence the work reported in this paper.

Acknowledgement

This work received funding from the China Scholarship Council and the Frontiers for the Future Programme of Research Ireland (grant number 21/FFP-P/10090). The authors gratefully acknowledge the valuable mentorship, support, and feedback from Prof. Herbert Einstein of the Department of Civil Engineering at the Massachusetts Institute of Technology.

Appendix A. Supplementary data

Supplementary data to this article can be found online at https://doi.org/10.1016/j.jrmge.2025.12.046.

References

AlDajani, O.A., 2022. Hydraulic Fracturing Behavior of Opalinus Shale: a Framework, Experimentation & Insights. Massachusetts Institute of Technology, Cambridge, USA. Doctoral dissertation.
Bergen, K.J., Johnson, P.A., de Hoop, M.V., Beroza, G.C., 2019. Machine learning for data-driven discovery in solid Earth geoscience. Science 363 (6433) eaau0323.
Basha, S.S., Dubey, S.R., Pulabaigari, V., Mukherjee, S., 2020. Impact of fully connected layers on performance of convolutional neural networks for image classification. Neurocomputing 378, 112–119.
Cameron, A.C., Windmeijer, F.A., 1997. An R-squared measure of goodness of fit for some common nonlinear regression models. J. Econom. 77 (2), 329–342.
Chang, S.H., Lee, C.I., 2004. Estimation of cracking and damage mechanisms in rock under triaxial compression by moment tensor analysis of acoustic emission. Int. J. Rock Mech. Min. Sci. 41 (7), 1069–1086.
Carpinteri, A., Corrado, M., Lacidogna, G., 2013. Heterogeneous materials in compression: correlations between absorbed, released and acoustic emission energies. Eng. Fail. Anal. 33, 236–250.
Christlein, V., Spranger, L., Seuret, M., Nicolaou, A., Král, P., Maier, A., 2019. Deep generalized max pooling. In: 2019 International Conference on Document Analysis and Recognition (ICDAR), pp. 1090–1096.
Cheng, T., Wang, L., Xiao, Y., He, M., Wang, T., Peng, M., Li, H., 2023a. Correlational fractal characteristics and damage progression of granite with different grain sizes based on acoustic emission monitoring. Eng. Geol. 327, 107358.
Cheng, T., He, M., Li, H., Liu, D., Qiao, Y., Hu, J., 2023b. Experimental investigation on the influence of a single structural plane on rockburst. Tunn. Undergr. Space Technol. 132, 104914.
Dresen, G., Stanchits, S., Rybacki, E., 2010. Borehole breakout evolution through acoustic emission location analysis. Int. J. Rock Mech. Min. Sci. 47 (3), 426–435.
Du, K., Li, X., Tao, M., Wang, S., 2020. Experimental study on acoustic emission (AE) characteristics and crack classification during rock fracture in several basic lab tests. Int. J. Rock Mech. Min. Sci. 133, 104411.
Dong, L., Shu, H., Tang, Z., Yan, X., 2023. Microseismic event waveform classification using CNN-based transfer learning models. Int. J. Min. Sci. Technol. 33 (10), 1203–1216.
Economides, M.J., Nolte, K.G., 2000. In: Reservoir stimulation, Vol. 18. Wiley, New York.
He, K., Zhang, X., Ren, S., Sun, J., 2016. Deep residual learning for image recognition. In: Proceedings of the IEEE Conference on Computer Vision and Pattern Recognition, pp. 770–778.
Kingma, D.P., Ba, J., 2014. Adam: A method for stochastic optimization. arXiv preprint arXiv:1412.6980.
Kuang, W., Yuan, C., Zhang, J., 2021. Real-time determination of earthquake focal mechanism via deep learning. Nat. Commun. 12 (1), 1432.
Lockner, D., 1993. The role of acoustic emission in the study of rock fracture. Int. J. Rock Mech. Min. Sci. Geomech. Abstracts 30 (7), 883–899.
Labuz, J.F., Carvalho, F.C., 2000. Post-failure micromechanisms in shear banding of rock. Acoustic Emission Beyond Millennium 145–158.
Labuz, J.F., Cattaneo, S., Chen, L.H., 2001. Acoustic emission at failure in quasi-brittle materials. Constr. Build. Mater. 15 (5-6), 225–233.
Li, Y.P., Chen, L.Z., Wang, Y.H., 2005. Experimental research on pre-cracked marble under compression. Int. J. Solid Struct. 42 (9-10), 2505–2516.
Li, B.Q., Moradian, Z., Goncalves da Silva, B., Germaine, J.T., 2015. Observations of acoustic emissions in a hydraulically loaded granite specimen. In: ARMA US Rock Mechanics/Geomechanics Symposium, pp. ARMA–2015.
Li, B.Q., da Silva, B.G., Einstein, H., 2019. Laboratory hydraulic fracturing of granite: acoustic emission observations and interpretation. Eng. Fract. Mech. 209, 200–220.

Lei, Q., Doonechaly, N.G., Tsang, C.F., 2021. Modelling fluid injection-induced fracture activation, damage growth, seismicity occurrence and connectivity change in naturally fractured rocks. Int. J. Rock Mech. Min. Sci. 138, 104598.

Li, M., Magsipoc, E., Abdelaziz, A., Ha, J., Peterson, K., Grasselli, G., 2022. Mapping fracture complexity of fractured shale in laboratory: three-dimensional reconstruction from serial-section images. Rock Mech. Rock Eng. 55 (5), 2937–2948.

Maxwell, S.C., Urbancic, T.I., Steinsberger, N., Zinno, R., 2002. Microseismic imaging of hydraulic fracture complexity in the Barnett shale. In: SPE Annual Technical Conference and Exhibition, pp. SPE–77440.

Moradian, Z.A., Ballivy, G., Rivard, P., Gravel, C., Rousseau, B., 2010. Evaluating damage during shear tests of rock joints using acoustic emissions. Int. J. Rock Mech. Min. Sci. 47 (4), 590–598.

Moradian, Z., Einstein, H.H., Ballivy, G., 2016. Detection of cracking levels in brittle rocks by parametric analysis of the acoustic emission signals. Rock Mech. Rock Eng. 49, 785–800.

Miao, S., Pan, P.Z., Wu, Z., Li, S., Zhao, S., 2018. Fracture analysis of sandstone with a single filled flaw under uniaxial compression. Eng. Fract. Mech. 204, 319–343.

Ohtsu, M., 2022. Moment tensor analysis. Acoustic Emission Testing: Basics for Research–Applications in Engineering, pp. 197–219.

Qiao, Y., Cheng, T., He, M., Li, H., Xiao, Y., Tang, J., 2024. Water content effect on borehole breakout in hard rock and its interpretation: an experimental study. Rock Mech. Rock Eng. 57 (9), 6715–6737.

Ross, Z.E., Meier, M.A., Hauksson, E., 2018. P wave arrival picking and first-motion polarity determination with deep learning. J. Geophys. Res. Solid Earth 123 (6), 5120–5129.

Rodríguez, P., Celestino, T.B., 2019. Application of acoustic emission monitoring and signal analysis to the qualitative and quantitative characterization of the fracturing process in rocks. Eng. Fract. Mech. 210, 54–69.

Shigeishi, M., Ohtsu, M., 2001. Acoustic emission moment tensor analysis: development for crack identification in concrete materials. Constr. Build. Mater. 15 (5-6), 311–319.

Sikdar, S., Liu, D., Kundu, A., 2022. Acoustic emission data based deep learning approach for classification and detection of damage-sources in a composite panel. Compos. B Eng. 228, 109450.

Song, Z., Zhang, Z., Zhang, G., Huang, J., Wu, M., 2022. Identifying the types of loading mode for rock fracture via convolutional neural networks. J. Geophys. Res. Solid Earth 127 (2) e2021JB022532.

Xie, A.Y., Li, B.Q., 2024. Transfer learning framework for multi-scale crack type classification with sparse microseismic networks. Int. J. Min. Sci. Technol. 34 (2), 167–178.

Yang, S.Q., Jing, H.W., 2011. Strength failure and crack coalescence behavior of brittle sandstone samples containing a single fissure under uniaxial compression. Int. J. Fract. 168, 227–250.

Yamashita, R., Nishio, M., Do, R.K.G., Togashi, K., 2018. Convolutional neural networks: an overview and application in radiology. Insights Imaging 9, 611–629.

Yu, Y., Si, X., Hu, C., Zhang, J., 2019. A review of recurrent neural networks: LSTM cells and network architectures. Neural Comput. 31 (7), 1235–1270.

Yuan, Z., Huang, H., Jiang, Y., Li, J., 2021. Hybrid deep neural networks for reservoir production prediction. J. Petrol. Sci. Eng. 197, 108111.

Zhao, Q., Lisjak, A., Mahabadi, O., Liu, Q., Grasselli, G., 2014. Numerical simulation of hydraulic fracturing and associated microseismicity using finite-discrete element method. J. Rock Mech. Geotech. Eng. 6 (6), 574–581.

Zha, W., Liu, Y., Wan, Y., Luo, R., Li, D., Yang, S., Xu, Y., 2022. Forecasting monthly gas field production based on the CNN-LSTM model. Energy 260, 124889.

Dr. Zili Li currently work as a Senior Lecturer (Associate Professor) in Geotechnical Engineering at University College Cork, Ireland. He also worked as a Visiting Professor / Affiliate Scholar at the Department of Civil and Environmental Engineering (CEE), Massachusetts Institute of Technology (MIT), USA since 2022. He is the chair of ISMLG 2023 (the 4th International Symposium of Machine Learning and Big Data in Geoscience), 29th August to September 1, 2023, University College Cork, Ireland. He is also the Leader of Task Force 'Big Data Acquisition' in TC309 Machine Learning & Big Data at the International Society for Soil Mechanics and Geotechnical Engineering (ISSMGE).